small methods
www.small-methods.com

# Disclosing the Redox Pathway Behind the Excellent Performance of CuS in Solid-State Batteries

*Angelo Mullaliu, Seyed Milad Hosseini, Paolo Conti, Giuliana Aquilanti, Marco Giorgetti, Alberto Varzi,* and Stefano Passerini**

**Copper sulfide has attracted increasing attention as conversion-type cathode material for, especially, solid-state lithium-based batteries. However, the reaction mechanism behind its extraordinary electroactivity is not well understood, and the various explanations given by the scientific community are diverging. Herein, the CuS reaction dynamics are highlighted by examining the occurring redox processes via a cutting-edge methodology combining X-ray absorption fine structure spectroscopy, and chemometrics to overcome X-ray diffraction limitations posed by the poor material's crystallinity. The mathematical approach rules out the formation of intermediates and clarifies the direct conversion of CuS to Cu in a two-electron process during discharge and reversible oxidation upon delithiation. Two distinct voltage regions are identified corresponding to Cu- as well as the S-redox mechanisms occurring in the material.**

## 1. Introduction

The global energy demand is constantly increasing, and the most used energy sources are still fossil fuels, which are the main reason for greenhouse gas emissions and global warming.[1] Despite being intrinsically intermittent, renewable sources such as wind and solar energies represent the solution to this fundamental problem. In this context, lithium-ion batteries (LIBs), as one of the leading technology for electrical energy storage, are crucial for stocking intermittent energy derived from renewable sources.[2,3] However, current LIBs, employing graphite as the negative electrode, a transition metal oxide as the positive electrode, and a carbonate liquid electrolyte, feature some drawbacks and limitations that need to be addressed for more sustainable energy storage and supply. Indeed, energy density is currently limited to 260 W h $kg^{-1}$[4] while safety, toxicity, and ethical issues are associated with inflammable liquid electrolytes and cobalt usage.[5–7]

As safer and more sustainable alternatives, solid inorganic electrolytes such as LiI-doped glassy $Li_2S$-$P_2S_5$, i.e., LPSI, and conversion materials such as transition metal sulfides (TMSs) have recently attracted wide attention. LPSI features high room temperature ionic conductivity of 1.2 mS $cm^{-1}$, and electrochemical and chemical compatibilities with lithium metal, whose adoption as anode material may result in a 40–50% energy density increase of the solid-state cell.[8] On the other hand, TMSs can deliver high capacities and provide long cycle life. We have previously reported the synergistic effect of incorporating LPSI and TMSs (CuS and $FeS_2$) in solid-state electrochemical cells with high areal capacity (2.5–3.5 mAh $cm^{-2}$), resulting in long-term cycling ability.[9,10] In particular, the high electronic conductivity (870 S $cm^{-1}$) and specific capacity (560 mAh $g^{-1}$)[11] make copper sulfide (CuS) exhibit a unique electrochemical performance in solid-state batteries, when employed as a composite cathode with carbon and LPSI.[10]

To understand the electrochemical behavior of conversion materials in solid-state batteries and, therefore, develop the next-generation batteries, a thorough investigation of the reaction dynamics needs to be conducted to determine the step-limiting factors, and optimize the electrochemical performance. In studies employing a liquid electrolyte, the first discharge process of CuS has been widely studied without, however, establishing a clear redox pathway. Eichinger et al.[12] assigned the first plateau observed upon the discharge to the CuS/Cu reduction (Equation (1)), and the second plateau to the solvent decomposition. Chung et al.,[13] instead, suggested the insertion

A. Mullaliu, S. M. Hosseini, A. Varzi, S. Passerini
Helmholtz Institute Ulm (HIU)
89081 Ulm, Germany
E-mail: alberto.varzi@kit.edu; stefano.passerini@kit.edu
A. Mullaliu, S. M. Hosseini, A. Varzi, S. Passerini
Karlsruhe Institute of Technology (KIT)
76021 Karlsruhe, Germany
P. Conti
School of Science and Technology
Chemistry Division
University of Camerino
Chemistry Interdisciplinary Project Building Via Madonna delle Carceri
62032 Camerino, Italy
G. Aquilanti
Elettra Sincrotrone Trieste
34149 Trieste, Italy
M. Giorgetti
Department of Industrial Chemistry "Toso Montanari"
University of Bologna
40136 Bologna, Italy
The ORCID identification number(s) for the author(s) of this article can be found under https://doi.org/10.1002/smtd.202200913.



**DOI: 10.1002/smtd.202200913**

of $Li^+$ into the CuS lattice in the first step (Equation (2)), followed by the conversion to metallic copper in the second step, involving the formation of djurleite ($Cu_{1.96}S$) as an intermediate reaction product. Similarly, Fournie et al.[14] assigned the first plateau to the insertion of $Li^+$ into the CuS lattice, but attributed the second one to a fast disproportionation (Equation (3)). On the other hand, Debart et al.[15] proposed a different reaction mechanism, where the intermediate formation of a wide variety of $Cu_{2-x}S$ polymorphs is followed by the reduction of CuS to $Cu_2S$, and final conversion to metallic copper and $Li_2S$ as the final discharge products. Furthermore, He et al.[16] proposed a displacement reaction for CuS nano-flakes under non-equilibrium conditions with Cu extrusion upon lithiation

$$CuS + 2Li^+ + 2e^- \rightarrow Cu + Li_2S \quad (1)$$

$$CuS + xLi^+ + xe^- \rightarrow Li_xCuS \quad (2)$$

$$Li_xCuS \rightarrow \frac{x}{2}Cu_2S + \frac{x}{2}Li_2S + (1-x)CuS \quad (3)$$

In solid-state batteries, the CuS reaction mechanism has not been extensively investigated.[17–20] Hayashi et al.[18] and Machida et al.[19] reported a similar potential profile, as the systems employing a liquid electrolyte agree through ex situ X-ray diffraction (XRD) with an insertion-conversion lithiation pathway. Using $Li_3PS_4$ solid electrolyte, Santhosha et al.[20] assigned the first potential plateau (2.1 V) to the conversion of CuS to $Cu_2S$ based on Debart and co-workers,[15] but confirmed the displacement reaction at the lower potential plateau (1.7 V), which leads to macroscopic phase separation of metallic copper and $Li_2S$ as final discharge products.

In our previous work,[10] we confirmed the formation of metallic copper based on ex situ XRD measurements. However, the poor crystallinity of the composite cathodes hindered any further detailed analysis. Herein, we overcome XRD's limitations and investigate the CuS reaction mechanism in a solid-state electrochemical cell by combining a chemometric technique, i.e., Multivariate Curve Resolution (MCR) analysis, with X-ray Absorption Fine Structure (XAFS). XAFS is a sophisticated and versatile characterization tool, often used in multielement systems to pinpoint a selected element's structural and electronic features. However, one of the current limitations regarding the analysis of the X-ray absorption near-edge structure (XANES) spectra is that it relies on qualitative or semi-quantitative methods based on the identification of pre-edge peaks, variations of the white line intensity, or shifts in the edge energy.[21] Moreover, extended X-ray absorption fine structure (EXAFS) analysis is time-consuming and the interpretation of in-situ datasets poses several challenges, such as the absence of reliable sequential data analysis. In this context, the joint MCR/XAFS approach is beneficial for analyzing in-situ data. Indeed, the MCR analysis helps to identify the pure spectral components present during the electrochemical cycling and their existence range, so that the XAFS analysis can be conducted only on a few relevant states of charge. In this work, the redox process is examined analytically by a well-defined methodology, clarifying the direct conversion of CuS to Cu in a two-electron process during discharge, and reversible oxidation upon delithiation. The reversible sulfur redox is also discussed.

## 2. Results and Discussion

First, the morphology of the composites was examined by scanning electron microscopy (SEM) and energy-dispersive X-ray spectroscopy (EDX). **Figure 1** compares six different compositions featuring different amounts of activated carbon and sulfide solid electrolyte (LPSI), while **Table 1** contains the weight compositions for all prepared composites. In the case of carbon-added composite electrodes, the intermediate composition, i.e., the binary CuS:C mixture after the first ball milling step, is also shown. The initial CuS particle size (cf. Figure 1a) reduces after ball milling, ranging from sub-micrometer to 5 µm. Activated carbon has smaller Mohs hardness (0.5–1) than CuS (1.5–2),[22,23] thus, CuS particles appear homogeneously covered with carbon after its addition amounting to 10 wt% (cf. Figure 1c,d) and 40 wt% (Figure 1e,f). Moreover, LPSI is ductile and soft, and blends uniformly with CuS upon ball milling, as evidenced by EDX (cf. Figure 1b,d,f).

Afterward, the composites' structural properties are investigated using XRD. The diffractograms of different binary mixtures of CuS and carbon are reported in Figure S3 in the Supporting Information. Upon ball milling, the patterns experience a broadening of the CuS reflections and an increasing background signal, especially for carbon content ≥50 wt%. **Figure 2**a, instead, shows the XRD patterns of the CuS/carbon/LPSI composites with a variable ratio of CuS/carbon, but constant LPSI (50 wt%). Broadly speaking, by increasing the amount of added carbon, thus, decreasing the amount of CuS at the same time, the background of the XRD pattern tends to increase and the peaks' intensity drops. Regardless of the composition, a small fraction of $Cu_6PS_5I$ or $Cu_yLi_{6-y}PS_5I$ is formed.[24–26] Despite several reflections' overlaps, a few distinct diffractions peak at 15.6°, 25.7°, 36.7°, and 45.3° (encompassed by rectangles in the figure) confirm the formation of the argyrodite compound. Indeed, driven by the high-energy ball milling, $Cu^+$ might partially replace $Li^+$ in LPSI since the two cations have very similar ionic radii ($Cu^+$ = 74 pm, $Li^+$ = 73 pm).[27] This is supported by a previous report by Chen et al., who observed a similar phenomenon during the discharge process which involves the formation of $Cu_yLi_{6-y}PS_5Br$ ($1.6 < y < 0.4$) when using $Li_6PS_5Br$ solid electrolyte.[17] We believe, however, that the formation of $Cu_6PS_5I$ is either minor or $y \ll 6$ in $Cu_yLi_{6-y}PS_5I$, as the XANES traces reported below do not reveal its presence, and the experimental Cu K-edge of the composite CuS electrode matches with that of pure CuS powder.

Furthermore, by comparing the patterns for increasing carbon content, no peaks shift or appearance of new reflections is observed, and the formation of $Cu_2S$ or any other non-stoichiometric $Cu_xS$ is excluded at a first glance. In fact, the very low crystallinity of the ball-milled mixtures hinders an accurate XRD interpretation and does not give precise insight into structural changes. Contrarily to XRD, which probes the long-distance order of materials, XAFS can be tuned to a specific element and elucidates its local environment. In this regard, adopting XAFS is necessary as it is element-selective and can

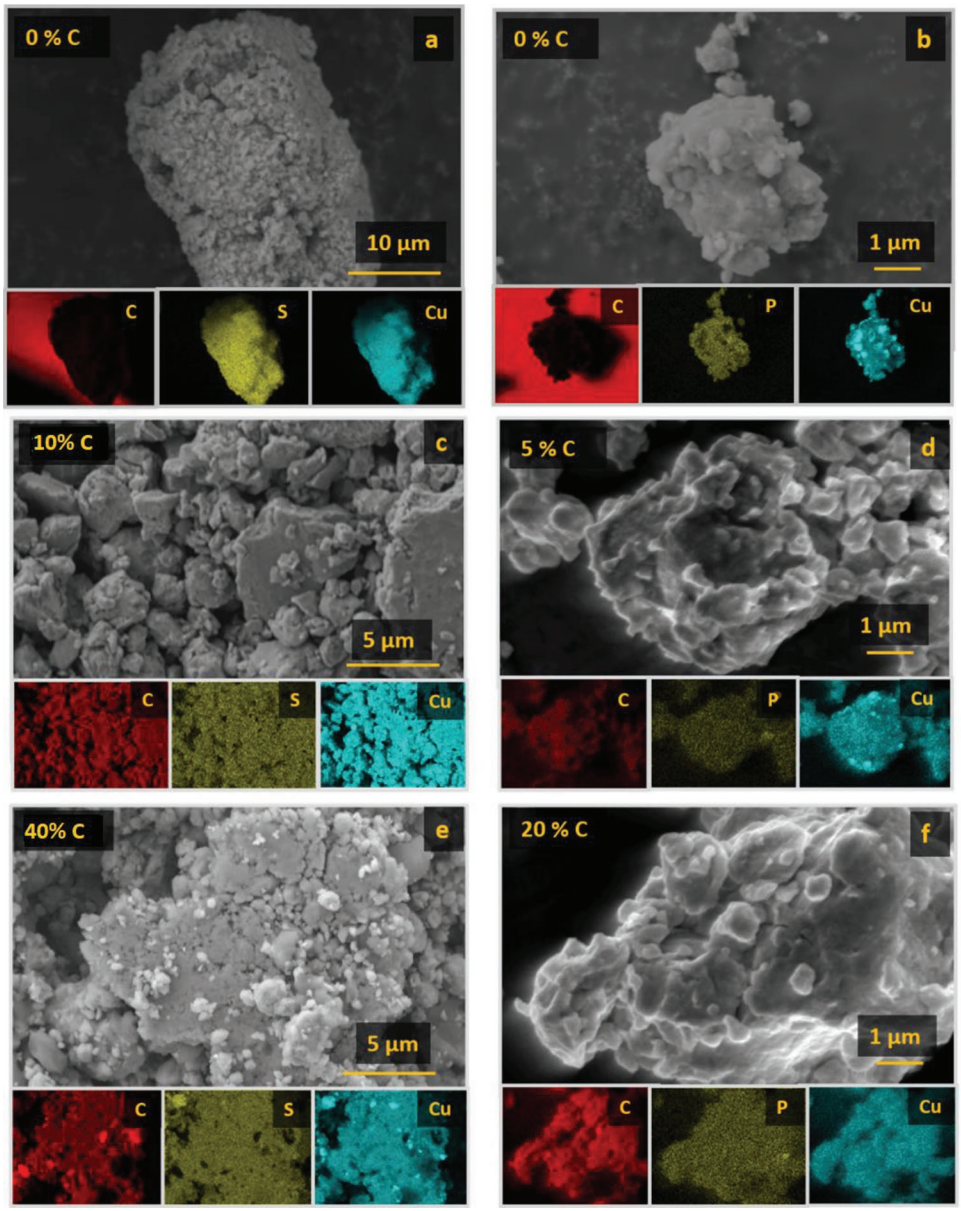


**Figure 1.** The SEM images and EDX maps. a) CuS powder as received. b) CuS ball-milled with 50 wt% LPSI (CuS:LPSI = 50:50) without carbon. The binary mixtures of CuS and c) 10 wt% (CuS:C = 90:10) and e) 40 wt% (CuS:C = 60:40) of carbon after the first ball milling step. In the second ball milling step, the CuS:C mixtures were added with 50 wt% LPSI, resulting in d) 5 wt% (CuS:C:LPSI = 45:5:50) and f) 20 wt% of carbon (CuS:C:LPSI = 30:20:50).

probe disordered materials, shedding light on the reaction mechanism of the CuS composites in solid-state cells.

The electrochemical characterization of the composite materials with different carbon amounts, ranging from 0 wt.% (CuS 00) to 25 wt.% (CuS 25) was carried out to assess the electrochemical behavior, and to establish the significance of performing an in-depth XAFS analysis on a few relevant samples. The composites were tested in solid-state Li|LPSI|CuS cells at 20 °C with a current of 0.2 mA $cm^{-2}$ unless otherwise stated. Figure 2b shows the first discharge voltage profile of the composites with different carbon content. The discharge capacity of the composites with 0 and 1 wt% carbon is very close to the theoretical specific capacity of CuS, whereas the delivered capacity decreases by 100–150 mAh $g^{-1}$ for higher amounts of carbon. Despite this initial disparity, the specific capacity gap between the high-carbon and low-carbon composites is already drastically reduced during the second discharge (Figure 2c), as the former experiences a significant electrochemical improvement. Indeed, the carbon content strongly influences the cycling performance of the Li|LPSI|CuS cells, as evidenced in Figure S5 (Supporting Information), and enhances the long-term cycling performance. The composite electrode with 20 wt% carbon displays extraordinary cycling performance against lithium metal for over 2000 cycles (cf. Figure S5, Supporting Information), showcasing excellent compatibility of the LPSI with lithium metal, and highly reversible de/lithiation of the cathode composite. The capacity fading

**Table 1.** Composition for the different composite cathode materials. For composites containing carbon, intermediate compositions, i.e., binary CuS:C mixtures, are also shown after the first ball milling step.

| Name | CuS [wt%] | C [wt%] | LPSI [wt%] |
|---|---|---|---|
| CuS 00 (CuS) | 50 | – | 50 |
| CuS 01 (intermediate) | 98 | 2 | – |
| CuS 01 | 49 | 1 | 50 |
| CuS 05 (intermediate) | 90 | 10 | – |
| CuS 05 | 45 | 5 | 50 |
| CuS 20 (intermediate) | 60 | 40 | – |
| CuS 20 (CuSC) | 30 | 20 | 50 |
| CuS 25 (intermediate) | 50 | 50 | – |
| CuS 25 | 25 | 25 | 50 |

of the composites with lower carbon content (<20 wt.%) might be related to the large volume expansion (70%) of CuS upon lithiation,[20] resulting in cracks and phase separation of the cathode composites as highlighted by the SEM images of the cycled electrodes (cf. Figure S5, Supporting Information). On the other hand, carbon can compensate for this massive stress on the cell, hindering the formation of cracks (cf. Figure S5, Supporting Information). Furthermore, from the cross-section EDX maps of the composites with 20 wt% carbon and without carbon (Figure S6, Supporting Information), copper appears to be homogeneously dispersed in the cathode layer in the presence of carbon, while larger particles tend to form in its absence as previously shown by Santhosha et al.[20] The formation of copper chunks may later result in high local current densities upon cycling and, thus, short-circuiting of the electrochemical cell.

Among the different composites, those with 0 and 20 wt% of carbon were chosen as representative datasets for further analysis, because of the pronounced difference in their electrochemical performance. In the following sections, they are referred to as CuS and CuSC, respectively.

The ex situ XAFS spectra were collected only at a few, but as relevant states of charge as displayed in **Figure 3**. Here, the selected states of charge are highlighted in the differential capacity plots for both CuS and CuSC in panels (a) and (b), respectively. The ex situ samples are labeled according to the notations X_Y where X is the dataset (CuS or CuSC), and Y is the potential value at which the electrodes were placed in open circuit conditions (OCV) prior to being taken out of the cells. CuS_p and CuSC_p, instead, define the pristine composite electrodes of the CuS and CuSC datasets, respectively. **Table 2** also indicates if the electrodes were stopped during charge or discharge, and the structural model used to describe the local environment of copper. Further explanation for the latter follows below.

### 2.1. Ex Situ XAFS Analysis

The Cu K-edge of CuS powder was first recorded to fine-tune the structural model for the ex situ samples. For this purpose,

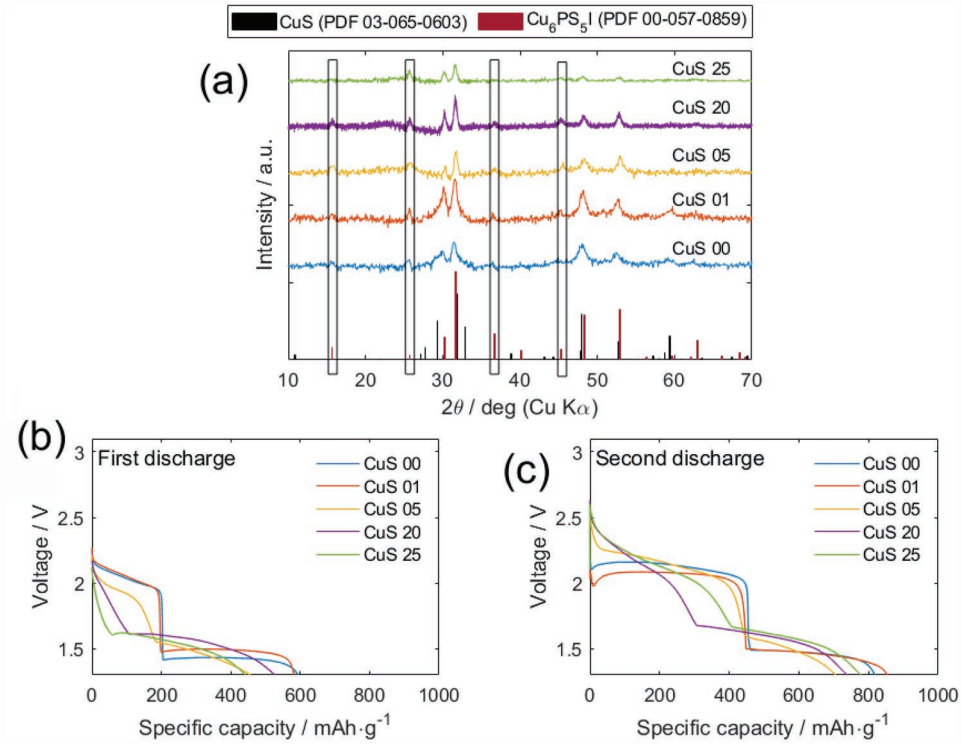


**Figure 2.** a) XRD patterns of cathode composites with different carbon content (CuS 00, CuS 01, CuS 05, CuS 20, CuS 25 include respectively 0 wt.%, 1 wt.%, 5 wt.%, 20 wt.% and 25 wt.% carbon) and constant LPSI content (50 wt.%). The peaks encompassed by black rectangles may correspond to an additional phase, i.e., $Cu_5PS_5I$ or $Cu_yLi_{6-y}PS_5I$. b) First and c) second discharge voltage profiles of composite cathodes at 20 °C with 0.2 mA $cm^{-2}$. The composites with higher carbon content also display the plateau at higher potentials in the second discharge step (panel c).

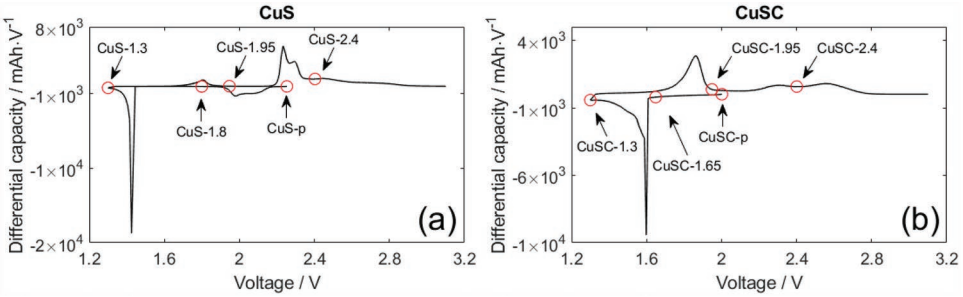


**Figure 3.** Differential capacity plots for a) CuS and b) CuSC. The ex situ XAFS investigated samples are indicated by the circles in panels (a) and (b).

EXAFS analysis of the CuS powder was performed considering the multiple scattering (MS) terms described in the Experimental Section and Scheme S1 (Supporting Information), i.e., $\gamma_a^{(2)}$ and $\gamma_b^{(2)}$. **Figure 4** compares the EXAFS's best-fit obtained using either two two-body terms (panels a and c) or only one two-body term (panels b and d). The experimental Fourier transforms (FTs) and EXAFS signals as wavenumber functions are well-fitted by the calculated signals in both cases. As it is seen from the figures, the fit does not considerably improve by using two $\gamma^{(2)}$ terms emphasizing the more decisive contribution of $\gamma_a^{(2)}$ to the overall signal, likely due to its higher degeneracy. Indeed, the $\gamma_a^{(2)}$ term has a degeneracy ≈2.7 times greater than $\gamma_b^{(2)}$ (cf. Scheme S1, Supporting Information), influencing the final EXAFS signal to a more considerable extent. Thus, the EXAFS signals can be described by only considering the $Cu^a - S^1$ fragment and disregarding the $Cu^b - S^2$ one. From here on, $Cu^a$–$S^1$ is referred to as $Cu^a$–S.

The CuSC_p sample displays some different features in the XANES spectrum compared to the CuS powder and CuS_p spectra (cf. Supporting Information). The CuSC_p edge is slightly shifted to lower energy values, suggesting that the carbon addition caused a partial alteration in the local structure or valence state. An explanation for this evidence is that carbon, as a reducing agent, might have partially reduced copper in CuS to its metallic form. However, the EXAFS analysis did not reveal any relevant contrast between the pristine powder and the composite electrodes before cycling, suggesting that the modification is minor and does not affect the overall copper local environment. As shown in Figure S10 (Supporting Information), the starting spectral shape of the operando CuSC dataset can be described as a CuS/Cu mixture, where the metallic fraction amounts to ≈6%.

**Figure 5** displays the recorded ex situ spectra for both sets of data, CuS and CuSC. Regarding CuS, the XANES of the pristine composite (CuS_p) and the cycled electrodes at 1.8 V (discharge) and 2.4 V (charge) look similar, except for some slight discrepancies around 8985 eV (cf. Figure 5a). The respective EXAFS portion of the spectra reported in panel c highlights a substantial structural similarity between CuS_p, CuS_1.8, and CuS_2.4 samples. This qualitative analysis suggests that these three samples can be described using the same EXAFS model, i.e., CuS, despite the expected different amounts of lithium in the structure. Indeed, Li does not affect the EXAFS signals significantly because of its weak scattering contribution. Moreover, it accentuates the overall reversibility experienced by the material upon cycling.

On the other hand, CuS_1.3 and CuS_1.95 samples are unrelated to the other ex situ CuS spectra, revealing the different electronic and structural features due to the presence of metallic copper. Although the XANES spectra at these states of charge, i.e., 1.3 V and 1.95 V, do not perfectly match, the EXAFS oscillations of the CuS_1.95 can be attributed to mixed contributions of a biphasic system. As a proof of this assumption, linear combination fitting (LCF) was conducted on the CuS_1.95 sample in the XANES portion (cf. Figure S9, Supporting Information). Accordingly, CuS_1.95 is a mixture of the initial state (represented by the spectrum of CuS powder) and the discharged state (CuS_1.3), i.e., metallic copper. More specifically, the sample under consideration predominantly consists of metallic copper, which contributes 82.7(9)% to the overall spectral shape, while only 17.3(9)% is attributable to CuS. Because of the prevalent metallic character, in a first approximation, the EXAFS analysis of CuS_1.95 was carried out as if the sample was made of only copper metal. The fit conducted by considering this assumption gave satisfactory results.

Considering the CuSC dataset, the spectral shape of CuSC_2.4 (stopped upon charge) well matches with the CuSC_1.65 (stopped in discharge), by displaying good reversibility. Furthermore, only CuSC_1.3 contains metallic Cu contributions, as highlighted by the EXAFS oscillations in panel d. Notably, CuSC_1.95 is entirely constituted of CuS, without any significant amount of copper metal. The spectral fingerprints of CuSC_1.95 and CuS_1.95 are in net contrast, implying that the two composites possess different reaction kinetics and that the electrochemical conversion from Cu to CuS during charge is faster for CuSC. In other words, the overpotential for CuS to return to the initial state decreases upon the addition of carbon.

**Table 2.** The ex situ XAFS investigated samples are reported in the table below, together with the adopted structural model.

| | CuS_p | CuS_1.8 | CuS_1.3 | CuS_1.95 | CuS_2.4 | CuSC_p | CuSC_1.65 | CuSC_1.3 | CuSC_1.95 | CuSC_2.4 |
|---|---|---|---|---|---|---|---|---|---|---|
| SOC | Pristine | Disch 1.8V | Disch 1.3V | Charge 1.95V | Charge 2.4V | Pristine | Disch 1.65V | Disch 1.3V | Charge 1.95V | Charge 2.4V |
| Model | CuS | CuS | Cu | Cu | CuS | CuS | CuS | Cu | CuS | CuS |

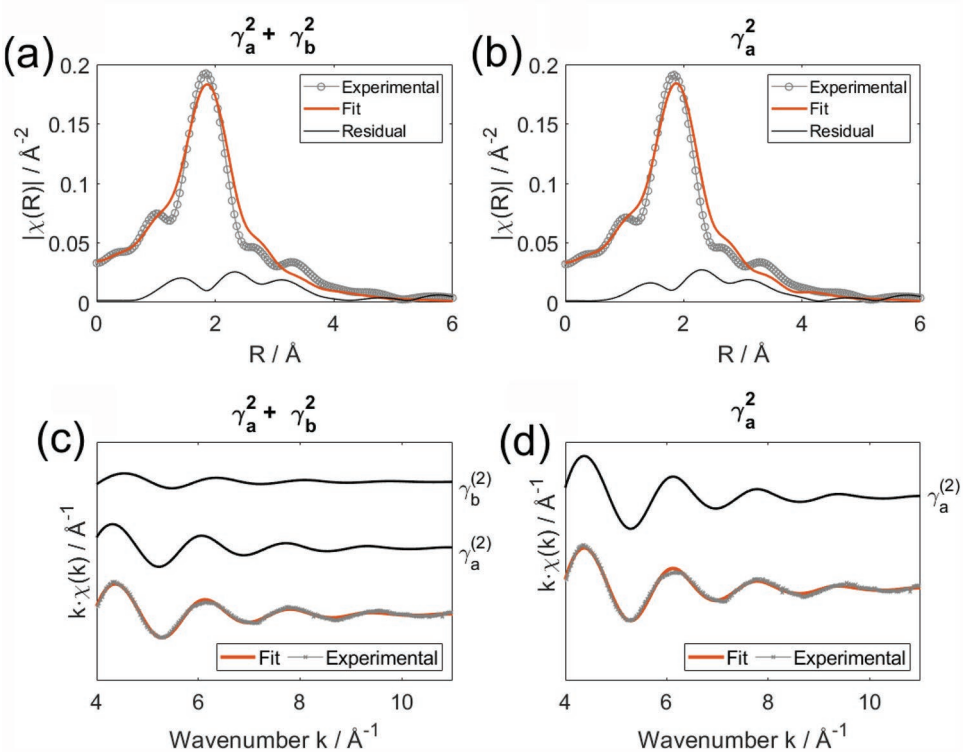


**Figure 4.** EXAFS best-fit for CuS powder using two $\gamma^{(2)}$ signals (panels a and c) and only one $\gamma^{(2)}$ signal (panels b and d). FTs of the EXAFS signal are displayed in (a) and (b), while the respective signals in $k \cdot \chi(k)$ are shown in (c) and (d).

Following the preliminary qualitative analysis, a quantitative evaluation of the ex situ samples was carried out by analyzing the EXAFS spectra. Concerning the samples that can be described using the CuS structural model, slight differences were found when comparing the two datasets. CuS and CuSC samples taken at the same state of charge do not differ significantly, apart from those collected during the first discharge before forming metallic copper, i.e., CuS_1.8 and CuSC_1.65 (cf. Figure S12, Supporting Information). Here, the Cu-S bond is shorter in CuSC, featuring a lower degree of disorder

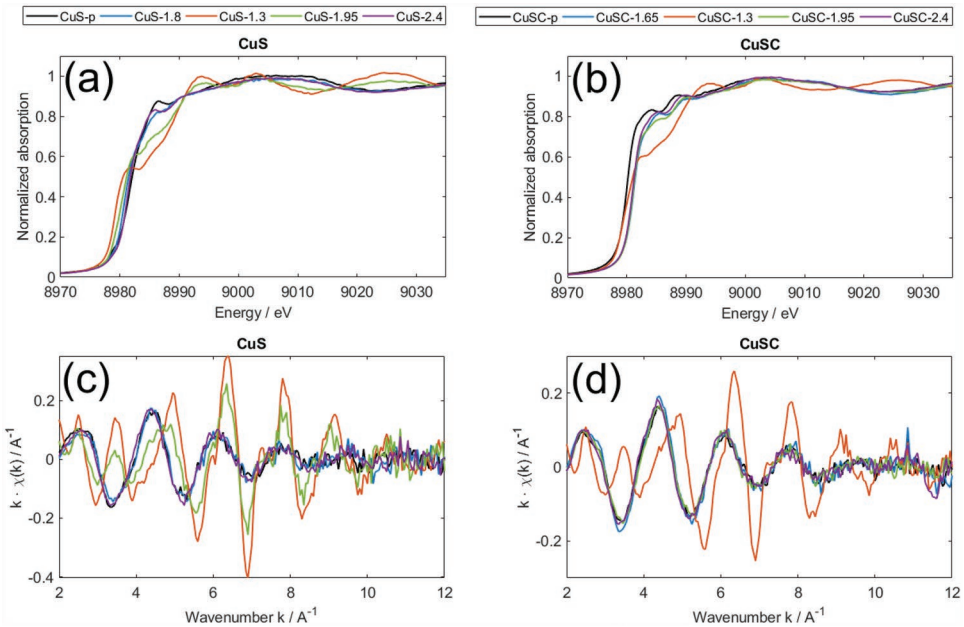


**Figure 5.** Ex situ XAFS spectra for the a,c) CuS and b,d) CuSC datasets. The upper panels (a,b) show the XANES spectra of both datasets at the selected states of charge, while the bottom panels (c,d) contain the respective EXAFS signal in $k \cdot \chi(k)$.

**Table 3.** The EXAFS fitting parameters for CuS_1.3, CuS_1.95, and CuSC_1.3 samples. DW stands for Debye-Waller. The two-body terms reported in the table are explained in detail in experimental section and Scheme S1 in the supporting information.

| Dataset | Sample | $\gamma_1^{(2)}$ | | $\gamma_2^{(2)}$ | | $\gamma_3^{(2)}$ | | Degeneracy[a)] | Defectivity[b)] |
|---|---|---|---|---|---|---|---|---|---|
| | | Distance [Å] | DW factor, $\sigma^2$ [Å$^2$] | Distance [Å] | DW factor, $\sigma^2$ [Å$^2$] | Distance [Å] | DW factor, $\sigma^2$ [Å$^2$] | | |
| CuS | 1.3 V | 2.546(2) | 0.0068(2) | 3.595(10) | 0.009(1) | 4.498(5) | 0.011(1) | 56% | 44% |
| | 1.95 V | 2.528(3) | 0.0070(3) | 3.540(20) | 0.013(3) | 4.483(9) | 0.015(1) | 37% | 63% |
| CuSC | 1.3 V | 2.530(3) | 0.0083(2) | 3.570(20) | 0.015(3) | 4.472(7) | 0.014(1) | 47% | 53% |

[a)]$\text{Degeneracy} = \frac{\text{Experimental signal multiplicity}}{\text{Theoretical signal multiplicity}} \cdot 100$. The value is obtained by simultaneously refining all MS signals; [b)]Defectivity = 1 − Degeneracy.

as evidenced by the Debye-Waller factors. Furthermore, CuSC_1.65 (discharge) and CuSC_2.4 (charge) have statistically equivalent Cu-S interatomic distances as the pristine CuSC_p, while the same does not hold for the CuS dataset. However, it is worth noticing that the maximum variation in the Cu-S distance upon cycling is ≈0.4%, underlining the material's high structural reversibility as the origin of its remarkable electrochemical performance.

A significant contrast between the CuS and CuSC sets can be detected, instead, for the remaining samples that are refined with the metallic Cu structural model. In this regard, **Table 3** contains the refined structural parameters of the CuS_1.3, CuS_1.95, and CuSC_1.3 samples. The fitting procedure was run twice by fixing the signals' multiplicities to the theoretical values and releasing them. Another way to visualize the signals' multiplicity is to consider the coordination sphere of metallic Cu. The $\gamma_1^2$ signal refers to the $Cu^0$–$Cu^1$ pair and has a theoretical multiplicity equal to 12 (cf. Scheme S1, Supporting Information); indeed, the $Cu^0$ coordination accounts for 12 equivalent $Cu^1$ at this distance. As shown in Figure S11 (Supporting Information), the fit on copper metal considerably improves by releasing the signals' multiplicities, which tend to assume much lower values than the theoretical one.

This data analysis introduced the degeneracy parameter,[28] defined as the percentage decrease in the signals' multiplicities with respect to the theoretical number, as expressed in Table 3. The degeneracy variable is retrieved in the algorithm minimization by considering all MS signals, meaning that the degeneracy of each signal (Scheme S1, Supporting Information) is reduced by the percentage extracted from the EXAFS analysis and presented in Table 3. The results delineate a substantial decrease in signals' degeneracy, suggesting a high defectivity (the degeneracy complement to unity) of the Cu local environment. Therefore, the in situ formed metal is remarkably different from the starting structural model and is, on average, ≈50% defective. When comparing samples at the same state of charge, CuSC_1.3 has higher defectivity than CuS_1.3 and is characterized by shorter Cu–Cu interatomic distances and higher Debye-Waller factors. Interestingly, CuS_1.95 appears more like CuSC_1.3 than the respective CuS sample within the calculated error (see also Supporting Information). This outcome might be related to the delay in reactivity of CuS (or the faster kinetics of CuSC) and agrees with the above considerations.

As revealed by LCF and discussed above, CuS_1.95 is constituted of 17% CuS, which might explain the highest Cu metal defectivity retrieved by the data analysis. The evidence of the CuS formation could indicate a transitory change and a low dimensionality of the Cu local structure, which evolves from 3D (100% Cu metal) to 2D-ish (83% Cu metal). The low dimensionality of the Cu local structure during CuS/Cu conversion is further sustained by ab initio simulations of the XANES spectra acquired during the operando experiment (cf. Figure S18, Supporting Information). Briefly, the CuS→Cu conversion involves the CuS lattice cleavage during discharge, and the experimental trend can be replicated by progressively decreasing the occupancy of the $Cu^a$ structural site. Therefore, the dimensionality of the Cu environment in the CuS lattice reduces because of the CuS cleavage and simultaneous Cu formation. Similar reasoning applies to the reverse Cu → CuS conversion, which explains the high Cu metal defectivity of CuSC_1.95. The dimensionality of metallic copper is supposedly diminished upon re-oxidation of CuS, as part of it is removed to form CuS.

### 2.2. Operando XANES and Reaction Dynamics

Operando XANES was performed on the CuSC sample due to its superior electrochemical performance and scientific interest in getting an insight into the reaction dynamics. The acquisition of the spectra was conducted in fluorescence mode, overcoming the high absorption of the solid electrolyte in the cell.

Upon a discharge/charge/discharge process, the electrochemical curve was acquired simultaneously with the XANES spectra at the Cu K-edge, as graphically displayed in (**Figure 6**a). The correspondence of the acquisition time, specific capacity, and spectrum number in the electrochemical curve is reported in Figure S14 (Supporting Information), while Figure 6b compares the XANES traces of the most relevant states of charge. The Multivariate Curve Resolution with Alternating Least Squares Algorithm (MCR-ALS) chemometric technique was used to further analyze the spectra, mathematically retrieving the number of pure spectral components during the operando experiment, without any a priori chemical or physical knowledge of the system.

The concentration profile plot of the pure spectral components upon cycling (Figure 6c) shows a progressive transformation of one species to another. The system evolves between two pure spectral components, labeled as "Species 1" and "Species 2" in Figure 6c,d. It can be deduced that the mathematically obtained spectra in Figure 5d belong to CuS and Cu,

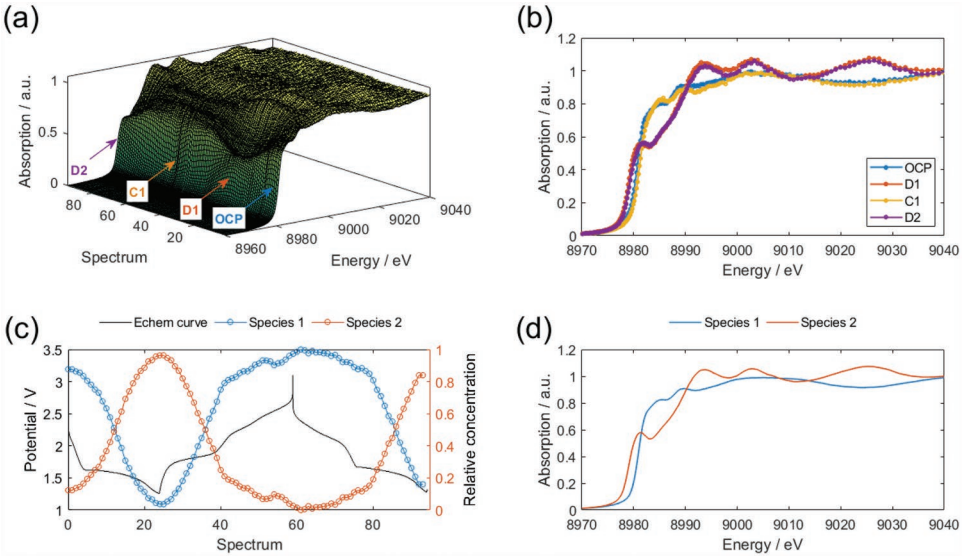


**Figure 6.** a) Graphical representation of all Cu K-edge spectra recorded during the electrochemical discharge/charge/discharge as a function of spectrum number (or time). b) A few selected spectra from the operando dataset are displayed: OCP was recorded before cycling, while D1, C1, and D2 correspond to the first discharged, first charged, and second discharged states, respectively. c) Concentration profile plot and d) pure spectral components retrieved by the MCR-ALS analysis of the operando XANES spectra. The profile plot is presented together with the electrochemical curve for better visualization of the reaction dynamics.

meaning that the electrochemical reaction does not involve any other Cu-based intermediate species. Indeed, three and four spectral components were also considered, but the analysis did not yield satisfactory results (cf. Supporting Information). Contrary to what other authors proposed, MCR-ALS unequivocally rules out intermediate species such as $Li_xCuS$ and $Cu_2S$. Thus, the EXAFS analysis of the ex situ samples and the following XANES interpretation must be conducted by considering only CuS and Cu as structural models. Fitting the signal with another Cu-based compound would mean disregarding the MCR results and, likely, overanalyzing the present dataset.

Furthermore, the starting spectrum (spectrum 0) partially contains metallic Cu. The LCF fitting on this state of charge independently reveals a 6% metallic contribution (cf. Supporting Information) that agrees with the MCR-ALS retrieved profile. Metallic Cu is supposedly present in the pristine electrode, as already suggested for the ex situ CuSC_p sample.

The concentration profile of the two pure spectral components can be further analyzed to give insight into the reaction dynamics, considering, for instance, the CuS/Cu conversion that occurs along the plateau of the first discharge process between spectra 5–24. Here, the CuS conversion follows a logarithmic law, and the reaction can be described with the Avrami–Erofeyev[29–31] equation (Equation (4)):

$$\left[-\ln(1-\alpha)\right]^{\frac{1}{n}} = k_1 t \tag{4}$$

where $\alpha$ is the conversion fraction, $n$ is a constant, $k_1$ is the rate constant, and $t$ is the reaction time.

The constant $n$ depends on the geometry of the conversion reaction and, in our case, is verified to be $n = 2$ (cf. Supporting Information), as expected for 2D disks and cylinders (as the electrode composite). Similarly, the Cu/CuS conversion and the CuS/Cu reaction in the second discharge follow the same logarithmic law expressed in Equation (4).

The same does not hold for the redox occurring above 2 V, where the conversion fraction $\alpha$ changes linearly with the acquisition time. In other words, the reaction dynamics in the upper-voltage window can be approximated with zero-order reaction kinetics, independent from the CuS concentration as follows (Equation (5)):

$$\alpha = k_2 t \tag{5}$$

Thus, the electrochemical reaction kinetics in the lower- and upper-voltage windows significantly varies and can be related to the different redox occurring upon cycling. Considering this experimental evidence, the electrochemical response can be rationalized with the following redox reactions. In the region below 2 V, the predominant reaction in the direction of oxidation can be written as

$$\mathrm{Cu} + (1-x)\,\mathrm{Li_2S} \rightleftharpoons \mathrm{CuS_{1-x}} + 2(1-x)\,\mathrm{Li^+} + 2(1-x)\,e^- \tag{6}$$

The Cu/CuS conversion also takes place above 2 V, as the amount of metallic Cu is non-zero. However, sulfur redox is believed to occur in this window primarily. From the reaction kinetics above 2 V, sulfur redox is not dependent on the CuS or Cu relative concentration, and the reaction can be written as

$$x\mathrm{Li_2S} \rightleftharpoons x\mathrm{S} + 2x\mathrm{Li^+} + 2xe^- \tag{7}$$

Therefore, the overall oxidation occurring during the charge is the sum of Equations (6) and (7):

$$\mathrm{Cu} + \mathrm{Li_2S} \rightleftharpoons \mathrm{CuS_{1-x}} + x\mathrm{S} + 2\mathrm{Li^+} + 2e^- \tag{8}$$

where $x \ll 1$. The spectral difference in CuS and $CuS_{1-x}$ is expected to be minor at the Cu K-edge for small values of $x$. Equation (8) describes the overall electrochemical reaction occurring during charge (and discharge if read in the opposite

direction). The only exception is the first discharge process, where CuS is converted into Cu according to Equation (6) with $x = 0$. Future studies may involve the complementary investigation of the S K-edge (≈2.4 keV) to detect any sulfur redox unambiguously; however, in this work, the high absorbance of the composite electrode renders the spectra acquisition unfeasible in this tender X-ray region.

## 3. Conclusions

The reaction mechanism of CuS composite cathodes in solid-state cells was investigated in detail. The addition of carbon is responsible for the exceptionally stable and long-term electrochemical performance. Ex situ XAFS analysis of the composites reveals that carbon acts as a reducing agent, as some metallic copper co-exists with CuS in the pristine composite prepared via ball-milling. Carbon boosts the electronic conductivity of the composite, thus the reaction kinetics, and increases the active material's homogeneity upon cycling, hindering the formation of cracks and enhancing mechanical stability. The operando acquisition of CuSC with the aid of MCR-ALS reveals that only two Cu-containing compounds are involved in the reaction, evidencing the presence of only CuS and metallic Cu upon cycling, and the absence of any other Cu-based compound, as $Cu_2S$ and Li-intercalated CuS. The voltage plateau above 2 V could be likely related to the sulfur redox, and its kinetics is independent of the amount of Cu or CuS, whereas the plateau at 1.6 V is due to the CuS conversion reaction to form the metallic Cu, and its kinetics depend on the amount of Cu or CuS, following first order-like reaction kinetics.

## 4. Experimental Section

*Material Preparation*: MAXSORB activated carbon (Kansai Coke and Chemicals Co., Ltd.), CuS (99.98%, Alfa-Aesar), LiI (Alfa Aeser, anhydrous, 99.95% metals basis), $Li_2S$ (Albemarle, 99.9% metals basis), and $P_2S_5$ (Sigma Aldrich, 99%), were dried and transferred to an Ar-filled UNIlab glove box (MBRAUN, $O_2$, and $H_2O < 0.1$ ppm). The LPSI was prepared via a solvent-assisted synthesis as previously reported.[32]

Several composite materials, see Table 1 for their compositions, were produced via ball-milling. The materials were weighed in the desired ratio and grounded in an agate mortar. Each mixture was then transferred in a 45 mL $ZrO_2$ jar filled with $ZrO_2$ balls (10 g of 1 mm balls, seventeen 5 mm balls, and ten 1 cm balls), sealed under an inert Ar atmosphere using parafilm and an additional clamping system to avoid exposure to air. Finally, the composite materials were ball-milled in a Pulverisette 4 (FRITSCH), alternating a ball-milling step at 360 rpm (45 min) with a rest (cooling) step (15 min). This procedure was repeated 17 times (total ball-milling time of ≈ 13 h). The jars were then transferred to an Ar-filled glove box, and the mixtures were recovered and separated from the $ZrO_2$ balls, grounded in an agate mortar, and mixed in a 1:1 weight ratio with the LPSI solid electrolyte. The CuS-C/SE mixtures were then transferred to a 45 mL $ZrO_2$ jar filled with $ZrO_2$ balls (10 g of 1 mm balls, seventeen 5 mm balls, and ten 1 cm balls), sealed under an inert Ar atmosphere using parafilm and an additional clamping system to avoid exposure to air. Finally, the mixtures were ball-milled in a Pulverisette 4 (FRITSCH), alternating a ball-milling step at 360 rpm (45 min) with a rest (cooling) step (15 min), and repeated 17 times to obtain the various composite electrode materials. These latter materials were recovered from the jar inside the Ar-filled glove box and grounded in an agate mortar prior to use for the electrochemical characterization.

*Cell Assembly*: An in-house, two-electrode (Ø = 13 mm) cell (Torque cell) was employed for cell assembly.[33,34] In detail, a cylindrical plastic case with an internal diameter of 13 mm was used as a die-set for pellet preparation. Lithium metal disks (thickness = 30 µm, Ø1.2 cm. Honjo Metal, Osaka) were used as the negative electrodes. About 300 mg of LPSI was introduced inside the die-set on top of the negative electrode disk and was pressed by a hydraulic press (YLJ-24, MTI corp.) at 2 MPa to form a pre-pellet. Afterward, a selected amount of the composite cathode material was spread over the electrolyte pre-pellet. The pre-formed cell was finally pressed at 10 MPa for 1 minute, at 20 °C, using the hydraulic press. The cell was hosted in a metal case equipped with a screw applying force on the upper current collector, ensuring the pelletized cell's mechanical stability, and helping to keep intimate contact between the materials. The cells were galvanostatically discharged to a specific voltage for ex situ samples and then transferred inside an Ar-filled glovebox. The pellets were recovered from the torque cells and vacuum-sealed in (polyethylene) bags for further experiments. For the operando measurement, a pellet-type cell was prepared and transferred inside a pouch-cell with Ni as a current collector, where the collector on the cathode side had a circular window with a 6 mm diameter that ensured the electronic contact to the active material, as well as free passage to the X-rays.

*Characterization*: Galvanostatic cycling tests were performed in the 1.3–3.1 V voltage range using a Maccor 4000 Battery Test System in thermostatic climatic chambers set at 20 °C, with a maximum deviation of ±1 °C. The cells were left to rest at OCV for 12 h before testing.

The morphological and structural characterizations of all materials were performed by a field emission SEM (Zeiss LEO1550VP Gemini) and XRD (Bruker D8 Advance diffractometer equipped with a $CuK_\alpha$ source $\lambda = 0.154$ nm). An air-tight, Ar-filled sample holder was used to transfer the samples from the glove box to the SEM chamber. Air-tight sample holders were employed to avoid sample degradation of the XRD measurements.

*XAFS Data Acquisition and Analysis*: XAFS experiments were performed at the XAFS beamline of Elettra – Sincrotrone Trieste (Italy).[35] The storage ring was operated at 2.0 GeV in top-up mode with a typical current of 310 mA. XAFS data was recorded at the Cu K-edge in fluorescence mode, using ionization chambers filled with a mixture of Ar, $N_2$, and He to have 10%, 70%, and 95% of absorption in the $I_0$, $I_1$, and $I_2$ chambers. Ex situ spectra were acquired from 8785 to 9727 eV around the Cu K-edge with a constant *k*-step of 0.03 $Å^{-1}$ with 2 s point acquisition time. Operando XANES spectra, instead, were collected from 8925 to 9117 eV.

The EXAFS analysis was performed using the GNXAS package[36,37] based on the MS theory. The sinusoidal signal of the experimental EXAFS spectra was described by considering only a few key contributions. The EXAFS spectra attributable to copper metal (cubic space group $Fm\bar{3}m$) were fitted with four relevant contributions, including three two-body ($\gamma^{(2)}$) term signals and one three-body ($\gamma^{(3)}$) term signal, following a reported fitting procedure.[28] As reported in Scheme S1 in the Supporting Information, the $\gamma^{(2)}$ terms were associated with three different pairs of copper atoms at different distances, i.e., 2.56 Å, 3.61 Å, and 4.43 Å, corresponding to the first-, second-, and third-shell contributions, respectively. The only $\gamma^{(3)}$ contribution used in the fitting procedure was associated with the $Cu^0$–$Cu^1$–$Cu^4$ triplet, being $Cu^0$ the photo absorber and $Cu^1$ and $Cu^4$ were the atoms placed in a straight line along the diagonal ($Cu^0$–$Cu^1$–$Cu^4$ = 180°), see Scheme S1, Supporting Information). This $\gamma^{(3)}$ term was included because of the so-called focusing effect and signal enhancement, due to the straight angle between the considered atoms. The three-body term also included a fourth two-body term, i.e., the $Cu^0$–$Cu^4$ contribution. The degeneracy of each signal is shown in Scheme S1 (Supporting Information). The high scattering of Cu atoms and the focusing effect allowed the inclusion of MS terms, unlike the fit on CuS.

The EXAFS spectra of CuS were fitted by considering the Cu–S $\chi^{(2)}$ terms associated with the two different Cu sites in the covellite structure (hexagonal space group P63/mmc). Indeed, the CuS lattice features two copper structural sites, namely $Cu^a$ and $Cu^b$, as shown in Scheme S1 (Supporting Information), that differed in content ($\frac{Cu^a}{Cu^b} = \frac{4}{2}$ per unit cell) and coordination geometry, as $Cu^a$ was tetra-coordinated and $Cu^b$ was tri-coordinated. In the covellite structure, sulfur atoms were either sulfide anions ($S^{2-}$, labeled as $S^2$) in a trigonal bipyramidal configuration (linking 2 $Cu^a$ and 3 $Cu^b$ atoms), or disulfide anions ($^-S–S^-$, each sulfur labeled as $S^1$) bridging $Cu^aS_4$ tetrahedra. In a first approximation for the calculation of the scattering signals, the environment of the $Cu^a$ site, consisting of $Cu^aS_3^1S_1^2$ polyhedra, is considered on average as $Cu^aS_4^1$ (ideal tetrahedron).

*Multivariate Curve Resolution with Alternating Least Squares Algorithm (MCR-ALS)*: MCR-ALS provides an additive bilinear model of pure contributions without any a priori information on the system,[38] decomposing the experimental matrix $X_{S,W}$ in a product of two matrices, as follows:

$$X_{S,W} = C_{S,F} \cdot A_{F,W} + E_{S,W} \quad (9)$$

where $C_{S,F}$ is the column matrix of the concentration profile, $A_{F,W}$ is the row matrix of the XANES spectra of pure species, and $E_{S,W}$ was the matrix of the residue.

The decomposition of the experimental matrix was achieved through evolving factor analysis,[38] which retrieved the number of pure species, as well as the first estimate of their concentration profiles required for initializing the ALS refinement. The closure condition and the non-negativity of both concentration and pure spectral components were used as constraints to obtain a unique and meaningful solution.

*Ab Initio XANES Simulations*: The ab initio simulation of the XANES spectra was performed using the FDMNES software.[39] The Cu K-edge was calculated in the photoelectron energy range $-5 < E < 120$ eV with respect to the Fermi energy level. The Hedin-Lundqvist complex potential[40] was used to calculate the excited states. The absorption cross-section was calculated within the dipolar approximation. Clusters of 5 Å built around each non-equivalent absorbing atom were considered. Space group symmetry was considered. The convolution parameters were kept constant for all spectra.

## Supporting Information

Supporting Information is available from the Wiley Online Library or from the author.

## Acknowledgements

The measurements at the Elettra – Sincrotrone, Basovizza (TS), Italy, were supported by Project no. 20195449 (A.M. as PI). The author acknowledges the Young Principal Investigator financial support conferred by SILS (Italian Society of the Synchrotron Radiation) as well as CALIPSOplus under Grant Agreement 730872 from the EU Framework Program for Research and Innovation HORIZON 2020. The HIU authors acknowledge the basic funding of the Helmholtz Association.

Open access funding enabled and organized by Projekt DEAL.

## Conflict of Interest

The authors declare no conflict of interest.

## Author Contribution

A.M. and S.M.H. contributed equally to this work. S.P., A.V., and A.M. conceived the study. S.M.H. carried out the electrochemical measurements and the physicochemical characterization. A.M., S.M.H., and G.A. performed the XAS experiments. A.M. and M.G. analyzed and interpreted the XAS data. P.C. performed the MCR-ALS analysis. A.M. and S.M.H. drafted the manuscript. All the authors discussed the results and commented on the manuscript.

## Data Availability Statement

The data that support the findings of this study are available on request from the corresponding author. The data are not publicly available due to privacy or ethical restrictions.

## Keywords

chemometrics, copper sulfide, EXAFS, lithium, solid-state batteries

Received: July 13, 2022
Revised: September 20, 2022
Published online:

[1] T. M. Gür, *Energy Environ. Sci.* **2018**, *11*, 2696.
[2] B. Dunn, H. Kamath, J.-M. Tarascon, *Science* **2011**, *334*, 928.
[3] D. O. Akinyele, R. K. Rayudu, *Sustain. Energy Technol. Assess* **2014**, *8*, 74.
[4] M. Armand, P. Axmann, D. Bresser, M. Copley, K. Edström, C. Ekberg, D. Guyomard, B. Lestriez, P. Novák, M. Petranikova, W. Porcher, S. Trabesinger, M. Wohlfahrt-Mehrens, H. Zhang, *J. Power Sources* **2020**, *479*, 228708.
[5] P. A. Christensen, P. A. Anderson, G. D. J. Harper, S. M. Lambert, W. Mrozik, M. A. Rajaeifar, M. S. Wise, O. Heidrich, *Renewable Sustain. Energy Rev.* **2021**, *148*, 111240.
[6] S. H. Farjana, N. Huda, M. A. P. Mahmud, *J. Sustain. Min.* **2019**, *18*, 150.
[7] M. Kuenzel, G.-T. Kim, M. Zarrabeitia, S. D. Lin, A. R. Schuer, D. Geiger, U. Kaiser, D. Bresser, S. Passerini, *Mater. Today* **2020**, *39*, 127.
[8] R. Weber, M. Genovese, A. J. Louli, S. Hames, C. Martin, I. G. Hill, J. R. Dahn, *Nat. Energy* **2019**, *4*, 683.
[9] U. Ulissi, S. Ito, S. M. Hosseini, A. Varzi, Y. Aihara, S. Passerini, *Adv. Energy Mater.* **2018**, *8*, 1.
[10] S. M. Hosseini, A. Varzi, S. Ito, Y. Aihara, S. Passerini, *Energy Storage Mater.* **2020**, *27*, 61.
[11] B. Jache, B. Mogwitz, F. Klein, P. Adelhelm, *J. Power Sources* **2014**, *247*, 703.
[12] G. Eichinger, H. P. Fritz, *Electrochim. Acta* **1975**, *20*, 753.
[13] J. S. Chung, H.-J. Sohn, *J. Power Sources* **2002**, *108*, 226.
[14] R. Fournie, R. Messina, J. Perichon, *J. Appl. Electrochem.* **1979**, *9*, 329.
[15] A. Débart, L. Dupont, R. Patrice, J.-M. Tarascon, *Solid State Sci.* **2006**, *8*, 640.
[16] K. He, Z. Yao, S. Hwang, N. Li, K. Sun, H. Gan, Y. Du, H. Zhang, C. Wolverton, D. Su, *Nano Lett.* **2017**, *17*, 5726.
[17] M. Chen, R. P. Rao, S. Adams, *Solid State Ion* **2014**, *268*, 300.
[18] A. Hayashi, T. Ohtomo, F. Mizuno, K. Tadanaga, M. Tatsumisago, *Electrochem. Commun.* **2003**, *5*, 701.
[19] N. Machida, K. Kobayashi, Y. Nishikawa, T. Shigematsu, *Solid State Ion* **2004**, *175*, 247.
[20] A. L. Santhosha, N. Nazer, R. Koerver, S. Randau, F. H. Richter, D. A. Weber, J. Kulisch, T. Adermann, J. Janek, P. Adelhelm, *Adv. Energy Mater.* **2020**, *10*, 2002394.
[21] J. Timoshenko, B. R. Cuenya, *Chem. Rev.* **2021**, *121*, 882.

[22] A. G. Patni, D. K. Ludlow, C. D. Adams, *J. Environ. Eng.* **2008**, *134*, 216.
[23] J. W. Anthony, R. A. Bideaux, K. W. Bladh, M. C. Nichols, *Handbook of Mineralogy*, Mineralogical Society of America, Chantilly, VA **2006**.
[24] I. P. Studenyak, V. O. Stefanovich, M. Kranjčec, D. I. Desnica, Y. M. Azhnyuk, G. S. Kovacs, V. V. Panko, *Solid State Ion* **1997**, *95*, 221.
[25] R. B. Beeken, J. J. Garbe, N. R. Petersen, *J. Phys. Chem. Solids* **2003**, *64*, 1261.
[26] W. F. Kuhs, R. Nitsche, K. Scheunemann, *Mater. Res. Bull.* **1976**, *11*, 1115.
[27] H.-J. Deiseroth, S.-T. Kong, H. Eckert, J. Vannahme, C. Reiner, T. Zaiß, M. Schlosser, *Angew. Chem., Int. Ed.* **2008**, *47*, 755.
[28] M. Giorgetti, S. Mukerjee, S. Passerini, J. McBreen, W. H. Smyrl, *J. Electrochem. Soc.* **2001**, *148*, 768.
[29] A. Khawam, D. R. Flanagan, *J. Phys. Chem. B* **2006**, *110*, 17315.
[30] S. Wang, Q. Gao, J. Wang, *J. Phys. Chem. B* **2005**, *109*, 17281.
[31] J. Graetz, J. J. Reilly, *J. Phys. Chem. B* **2005**, *109*, 22181.
[32] S. M. Hosseini, A. Varzi, T. Tsujimura, Y. Aihara, S. Passerini, *Energy Technol.* **2021**, *9*, 2100385.
[33] S. Ito, S. Fujiki, T. Yamada, Y. Aihara, Y. Park, T. Y. Kim, S.-W. Baek, J.-M. Lee, S. Doo, N. Machida, *J. Power Sources* **2014**, *248*, 943.
[34] U. Ulissi, M. Agostini, S. Ito, Y. Aihara, J. Hassoun, *Solid State Ion* **2016**, *296*, 13.
[35] G. Aquilanti, M. Giorgetti, R. Dominko, L. Stievano, I. Arčon, N. Novello, L. Olivi, *J. Phys. D: Appl. Phys.* **2017**, *50*, 074001.
[36] A. Filipponi, A. D. Cicco, C. R. Natoli, *Phys. Rev. B* **1995**, *52*, 15122.
[37] A. Filipponi, A. D. Cicco, *Phys. Rev. B* **1995**, *52*, 15135.
[38] A. de Juan, J. Jaumot, R. Tauler, *Anal. Methods* **2014**, *6*, 4964.
[39] Y. Joly, *Phys. Rev. B: Condens. Matter Mater. Phys.* **2001**, *63*, 125120.
[40] L. Hedin, B. I. Lundqvist, S. Lundqvist, *Solid State Commun.* **1971**, *9*, 537.